LAWRENCE
LIVERMORE
NATIONAL
LABORATORY

LLNL-JRNL-507611

Adiabatic index in shock-compressed Be

S. H. Glenzer, C. Fortmann, H. J. Lee, T. Doeppner, R. W. Falcone, A. L. Kritcher, O. L. Landen

October 21, 2011

Contributions to Plasma Physics

Disclaimer

Adiabatic index in shock-compressed Be

Carsten Fortmann[1,2*], **Hae Ja Lee**[3], **Tilo Döppner**[1], **Roger W. Falcone**[4], **Andrea L. Kritcher**[1], **Otto L. Landen**[1], **Christoph Niemann**[2], and **Siegfried H. Glenzer**[1]

[1] Lawrence Livermore National Laboratory, PO Box 808, L-493, Livermore CA 94551, USA
[2] Departement of Physics and Astronomy, University of California Los Angeles, Los Angeles CA 90095, USA
[3] SLAC National Accelerator Laboratory, 2575 Sand Hill Rd. Menlo Park, CA 94025
[4] Department of Physics, University of California, Berkeley, CA 94720, USA

Key words X-Ray Thomson Scattering, counterpropagating shocks, heat capacity ratio, equation of state

We present a method to measure the adiabatic index of a material under shock compression by X-ray Thomson Scattering. A Beryllium target is symmetrically compressed by two counterpropagating shock waves that collide in the target center, producing super dense states of matter of up to 6 fold compression. We measure the density before and after the shock collision and solve the Hugoniot relations for colliding shocks to infer the adiabatic index. Our results indicate that the adiabatic index stays rather high even in the high compression regime. This agrees with a linear scaling model taken from the SESAME equation of state and shows that the adiabatic index becomes significantly different from the ratio of heat capacities in this strongly coupled plasma.

1 Introduction

Measurement of static and dynamic properties of shock compressed matter has become an important technique to characterize materials under extreme conditions of pressure, density, and temperature, relevant for astrophysical applications and inertial confinement fusion. X-ray Thomson scattering [1] was demonstrated to provide accurate measurements of the electron density, electron temperature, ionization and ionic structure for a wide variety of isochorically heated, and shock-compressed materials. Beryllium has received special attention as a candidate ablator material for inertial confinement fusion capsules in the indirect drive scheme [2].

Of particular interest to equation of state research are the adiabatic exponents. Adiabatic exponents characterise isentropic changes (entropy $S = \text{const.}$) in the thermodynamic state of a system with the general equation of state $f(p, \rho, T) = 0$ [3], such a shock compression. Correspondingly, there are three adiabatic indices, $\gamma_1 = (\partial \ln p/\partial \ln \rho)_S$, also called the *sound speed gamma*, $\gamma_2/\gamma_2 - 1 = (\partial \ln p/\partial \ln T)_S$, and $\gamma_3 = 1 + (\partial \ln T/\partial \ln \rho)_S$. For shock wave applications, it is useful to introduce the *shock gamma* $\gamma_{\text{sh}} = 1 + p/\rho\varepsilon$, with the internal energy density ε. In general, the adiabatic exponents and the shock gamma themselves depend on pressure, temperature, and density, and are not equal to each other. Except for the perfect gas of non-interacting particles obeying Maxwell-Boltzmann statistics, we have $\gamma_1 = \gamma_2 = \gamma_3 = \gamma_{\text{sh}} = c_p/c_v$, the ratio of heat capacities at constant pressure and volume, respectively. E.g. for an ideal Fermi gas of non-interacting quantum particles, this is no longer true, as the heat capacity ratio is $(c_p/c_v)_{\text{FG}} = 1$, whereas in the classical monoatomic gas $(c_p/c_v)_{\text{cl}} = 5/3$.

In this paper, we describe a method to determine the shock gamma as a function of density at ultrahigh compression ratios exceeding the single shock compression limit $\rho/\rho_0 = (\gamma_{\text{sh}} + 1)/(\gamma_{\text{sh}} - 1)$ by measuring the density before and after the collision of two equal shock waves. For this special setup, one can solve the Hugoniot relations between pressure, shock velocity, and mass density using that the material velocity vanishes at the shock front interface at the moment of shock collision.

The paper is organized as follows: In the following section we will briefly outline the derivation of the Hugoniot relations for colliding shock waves and show how the shock gamma can be determined if the compression ratios before and after collision are measured. In Sec. 3 we describe the experiment and discuss the X-Ray Thomson Scattering results for electron density, temperature, and ionization. Results for the shock gamma are

* Corresponding author E-mail: fortmann1@llnl.gov, Phone: +1 925 423 0152

presented in Sec. 4 and Sec. 5 discusses effects of the density dependence of γ_{sh} on the maximum single shock compressibility compared to models that assume a constant γ.

2 Shock wave kinematics with density dependent γ

2.1 Single planar shock waves

The propagation of a planar shock front through matter is commonly described by the Hugoniot relations [4], that relate the conditions before and after the shock front to the shock front velocity U. The Hugoniot relations are derived from the conservation of mass, momentum, and energy in a small volume that extends across the shock front, and which in the reference frame of the shock front read

$$u_0\rho_0 = u_1\rho_1 \ , \tag{1a}$$

$$u_0^2\rho_0 + p_0 = u_1^2\rho_1 + p_1 \ , \tag{1b}$$

$$u_0^2\rho_0 + \rho_0\varepsilon_0 + p_0 = u_1^2\rho_1 + \rho_1\varepsilon_1 + p_1 \ . \tag{1c}$$

Here, $u_i = v_i - U$ are the particle velocities with respect to the shock front, $p_i, \rho_i, \varepsilon_i$ are pressure, mass density, and energy density, respectively, and index 0 denotes conditions ahead of the shock front, i.e in the uncompressed material, index 1 denotes the conditions in the compressed material, behind the shock front. After some algebra, the Hugoniot relation is established,

$$\varepsilon_0 - \varepsilon_1 = \frac{1}{2}\left(p_0 + p_1\right)\left(1/\rho_1 - 1/\rho_0\right) \ , \tag{2}$$

We replace the energy densities $\varepsilon_0, \varepsilon_1$ by

$$\varepsilon_i = \frac{p_i}{\left(\gamma_i - 1\right)\rho_i} \ , i = 0, 1. \tag{3}$$

Here and in the following, $\gamma = \gamma_{\text{sh}}$ is the shock gamma if not stated otherwise. The resulting equation

$$\frac{p_0}{\left(\gamma_0 - 1\right)\rho_0} - \frac{p_1}{\left(\gamma_1 - 1\right)\rho_1} = \frac{1}{2}\left(p_0 + p_1\right)\left(1/\rho_1 - 1/\rho_0\right) \ , \tag{4}$$

is solved for the compression ratio $x_{01} = \rho_1/\rho_0$ as a function of the shock strength $z_{01} = (p_1 - p_0)/p_0$,

$$x_{01} = \frac{1 + \left(1 + z_{01}\right)\frac{\gamma_1+1}{\gamma_1-1}}{1 + z_{01} + \frac{\gamma_0+1}{\gamma_0-1}} \ . \tag{5}$$

For a strong shock $p_1 \ll p_0, z_{01} \ll 1$, one immediately finds the well known result

$$x_{01} = \frac{\gamma_1 + 1}{\gamma_1 - 1} \ . \tag{6}$$

Note that the strong shock compression depends only on the equation of state of the compressed material represented by γ_1.

For later use, we solve Eq. (5) for the shock strength,

$$z_{ij} = 2\frac{\gamma_j - x_{ij}\gamma_i\frac{\gamma_j-1}{\gamma_i-1}}{x_j\left(\gamma_j - 1\right) - \gamma_j - 1} \tag{7}$$

2.2 Colliding Shock waves

Upon collision of two shock waves, two new shock fronts separating single shocked from twice shocked material evolve that travel away from each other. The situation is equivalent to the reflection of a single shock on an infinitely rigid wall, which is treated in Ref. [5] for the case of constant γ. Here, the more general case of γ being itself density dependent, is treated. The final state in the double shocked material is completely determined by the initial shock strength. Indeed, as the following analysis will show, the effective shock strength $z_{12} = p_2/p_1 - 1$ and hence the second compression ratio $x_{12} = \rho_2/\rho_1$ can be expressed uniquely as functions of the initial shock strength z_{01}, i.e. the first compression ratio x_{01}. We rewrite the continuity equation Eq. (1a)

$$u_0 - u_1 = u_1 \left(\frac{\rho_1}{\rho_0} - 1 \right) = u_1 \left(x_{01} - 1 \right) \ , \tag{8}$$

and the conservation of energy Eq. (1c) as

$$u_1^2 = \frac{p_1 - p_0}{\rho_1 - \rho_0} \frac{\rho_0}{\rho_1} \ , \tag{9}$$

such that Eq.(8) becomes

$$\begin{aligned} u_0 - u_1 &= \left(\frac{p_1 - p_0}{\rho_1 - \rho_0} \frac{\rho_0}{\rho_1} \right)^{1/2} \left(\frac{\rho_1}{\rho_0} - 1 \right) \\ &= \left(\frac{p_0}{\rho_0} \frac{z_{01}}{\left(x_{01} - 1 \right) x_{01}} \right)^{1/2} \left(x_{01} - 1 \right) . \end{aligned} \tag{10}$$

Clearly, the same equation can be derived for $u_1 - u_2$,

$$u_1 - u_2 = \left(\frac{p_1}{\rho_1} \frac{z_{12}}{\left(x_{12} - 1 \right) x_{12}} \right)^{1/2} \left(x_{12} - 1 \right) \ . \tag{11}$$

Now, $u_0 - u_1 = v_0 - v_1$ with $v_0 = U + u_0, v_1 = U + u_1$ the velocities in the laboratory system. Making the approximation that the material is initially at rest $v_0 = 0$, and that the material at the contact interface is also at rest, $v_2 = 0$, we can combine the ride-hand-sides of Eq.(10) and Eq.(11),

$$\frac{p_0}{\rho_0} \left(\frac{z_{01}}{\left(x_{01} - 1 \right) x_{01}} \right)^{1/2} \left(x_{01} - 1 \right)^2 = \frac{p_1}{\rho_1} \left(\frac{z_{12}}{\left(x_{12} - 1 \right) x_{12}} \right)^{1/2} \left(x_{12} - 1 \right) \ . \tag{12}$$

After some manipulation this yields the second shock strength z_{12} as a function of $x_{12}, x_{01},$ and z_{01},

$$z_{12} = x_{12} \frac{x_{01} - 1}{x_{12} - 1} \frac{z_{01}}{1 + z_{01}} \ . \tag{13}$$

Eliminating z_{12} through x_{12} (see Eq. (7)), we find

$$x_{12} \frac{x_{01} - 1}{x_{12} - 1} \frac{z_{01}}{1 + z_{01}} = 2 \frac{\gamma_2 - x_{12} \gamma_1 \frac{\gamma_2 - 1}{\gamma_1 - 1}}{x_{12} (\gamma_2 - 1) - \gamma_2 - 1} \ , \tag{14}$$

and, after resubstituting x_{01} as function of z_{01}, finally

$$\frac{x_{12}}{x_{12} - 1} \frac{z_{01}}{1 + z_{01}} \frac{\left(1 + z_{01} \right) \frac{\gamma_1 + 1}{\gamma_1 - 1} - z_{01} - \frac{\gamma_0 + 1}{\gamma_0 - 1}}{1 + z_{01} + \frac{\gamma_0 + 1}{\gamma_0 - 1}} = 2 \frac{\gamma_2 - x_{12} \gamma_1 \frac{\gamma_2 - 1}{\gamma_1 - 1}}{x_{12} (\gamma_2 - 1) - \gamma_2 - 1} \ . \tag{15}$$

This equation can be solved for x_{12}, the formula is given in the appendix.

In the strong shock limit $z_{01} \ll 1$ and $x_{01} = (\gamma_1 + 1) / (\gamma_1 - 1)$ this reduces to a second order equation for x_{12} with one physically meaningful ($x_{12} > 1$) solution

$$x_{12} = \frac{\gamma_2}{\gamma_2 - 1} \ . \tag{16}$$

Also for the second shock front, the compression ratio depends only on the adiabatic index in the final state of the material. In the perfect gas ($\gamma = 5/3$), we have $x_{23} = 2.5$, hence the compression after shock collision with respect to the uncompressed state is $\rho_2/\rho_0 = 4 \cdot 2.5 = 10$.

In consequence, by measuring the mass density before and after the shock collision ρ_1 and ρ_2, i.e. in the single and in the double shocked material, we can determine the adiabatic index as a function of mass density for up to 10 times compression. Solving Eqs (6) and (16) for γ_1 and γ_2, we have

$$\gamma_1 = \frac{\rho_1 + \rho_0}{\rho_1 - \rho_0} \tag{17a}$$

$$\gamma_2 = \frac{\rho_1}{\rho_2 - \rho_1} \tag{17b}$$

3 Measurement of the electron density

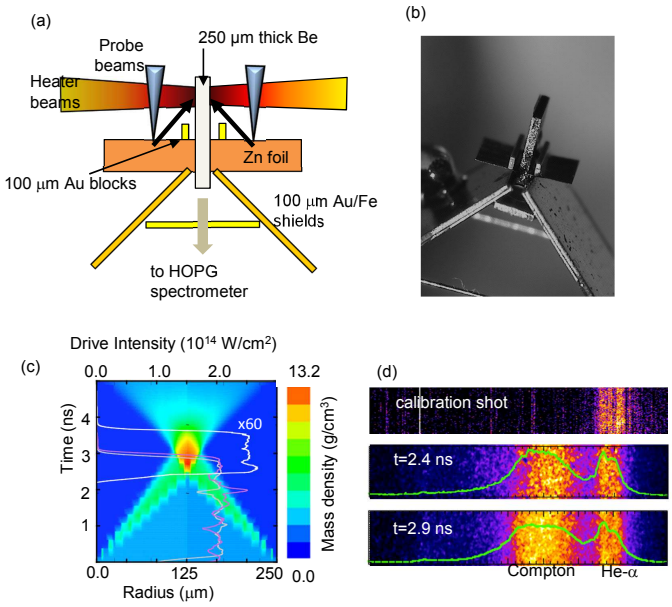

Fig. 1 (Color online) (a) Schematic of experiment showing compression drive beams and x-ray probe beams. (b) Photograph of the target (c) Rad-hydro simulation of the mass density evolution as function of target depth. The drive beam intensity profiles for each side (grey and purple) and the x-ray probe pulse (white, scaled by factor 1/60) are overlayed. (d) Raw x-ray scattering data measured in the HOPG spectrometer, energy dispersion is in horizontal direction. Top to bottom: Calibration shot, measuring the Zn He-α doublet; scattering data before shock collision showing elastic and Compton scattering; increased Compton width is observed after after shock collision. Green: spectral lineouts.

In our experiment, performed at the Omega laser at Laboratory for Laser Energetics, we measured the electron density, temperature, and ionization by time-resolved non-collective X-ray Thomson Scattering (Compton Scattering). The experimental setup is shown in Fig. 1(a). A $250\,\mu$m thick high purity beryllium foil ($< 0.2\%$ contaminations) is symmetrically irradiated by a total of 20 laser beams at 351 nm wavelength. Each laser carries 480 J in a 1 ns long pulse, the pulses are staggered in time and focussed on $800\,\mu$m diameter focal spot, yielding a flat top intensity profile of 2.4×10^{14} W/cm^2 for 3 ns on the target surface, see Fig. 1(c). Use of continuous phase plates (CPP) ensures a homogeneous intensity profile across the focus. The interaction of the intense laser with the beryllium target is modelled with the radiation-hydrodynamics code HELIOS [6]. The mass density as function of target depth and of time is shown in Fig. 1(c). The two shock waves collide after ~ 2.8 ns in the target center creating ultra-high density states of matter at mass densities of ~ 13 g/cm^3 according to the simulation.

The conditions in the single shocked and in the double shocked material are probed by intense Zn He-α radiation (9 keV photon energy). Two sets of laser beams are focussed on a 200 μm diameter spot on a Zn foil, see Fig. 1(a). Pulses of 1 ns duration and 480 J pulse energy yield intensities of 1.5×10^{16} W/cm^2, see Fig. 1(c). Zn He-α radiation penetrates deep into the compressed Be. The scattered radiation (scattering angle $\theta = 140^\circ \pm 10^\circ$) is spectrally dispersed in a highly oriented pyrolytic graphite (HOPG) crystal and detected in a x-ray framing camera with a time resolution of 0.18 ns. Raw data from before shock collision ($t = 2.4$ ns) and immediately after shock collision ($t = 2.9$ ns) are shown in Fig. 1(d) together with data from a calibration shot measuring only the Zn He-α radiation at 9 keV. Besides Rayleigh (elastic) scattering from tightly bound K-shell electrons, Compton scattering produces an additional feature that is red-shifted from the elastic signal by the Compton shift $E_C = \hbar^2 k^2 / 2 m_e \simeq 270$ eV, where $k = 2E_0/\hbar c \sin\theta/2 = (8.4 \pm 0.2)$ Å^{-1} is the transfer wavenumber.

In Fig. 1(d) we also show spectral lineouts from the raw data. Clearly, the Compton width in the post-collision data is increased with respect to the pre-collision data.

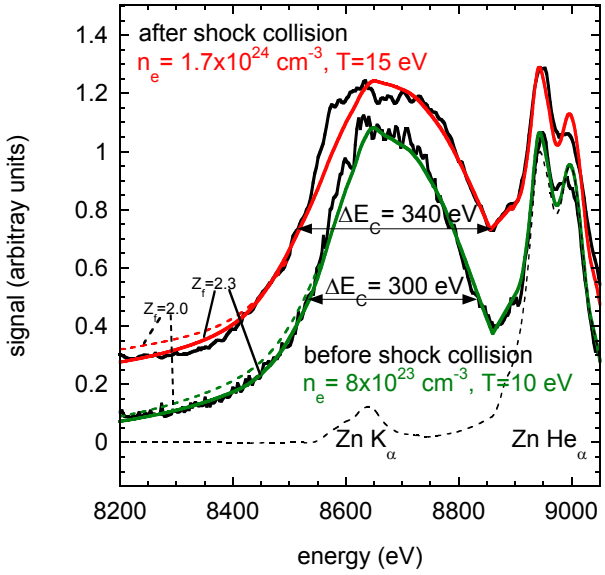

Fig. 2 (Color online) X-ray scattering spectra measured before shock collision at $t = 2.4$ ns and after shock collision at $t = 2.9$ ns (including a 0.2 vertical offset). Red and green curves represent Thomson scattering simulations for the best-fit values for electron density of $n_e = 8.0 \times 10^{23}$ cm^{-3} and temperature $T = 10$ eV and $n_e = 1.7 \times 10^{24}$ cm^{-3}, $T = 15$ eV before and after shock collision, respectively. Also shown is the x-ray probe (Zn He$_\alpha$) spectrum and the Zn K$_\alpha$ line that was measured seperately and which is included in the theoretical calculations . $Z_f = 2.3$ is used in both calculations, thin dashed lines were calculated with $Z_f = 2.0$.

The spectra are corrected for inhomogeneities in the HOPG reflectivity ("flatfielding") and a linear background is subtracted. These spectra are shown in Fig. 2 together with best fit calculations for the dynamical structure factor. The dynamical structure factor

$$S(k,\omega) = |f(k) + q(k)|^2 S_{ii}(k,\omega) + Z_f S^0_{ee}(k,\omega) + Z_c S_{ce}(k,\omega) \tag{18}$$

describes the differential scattering cross-section in a partially ionized plasma with elastic scattering from tightly bound electrons and free electrons screening the ion charge (first term in (18)) as well as inelastic scattering from free electrons (second term) and from bound electrons (third term). In Eq. (18), $f(k)$ and $q(k)$ are the form factors for bound electrons and for free electrons, respectively, Z_f and Z_c are the number of free and core electrons per ion, and S_{ii}, S^0_{ee}, and S_{ce} are the structure factors for ions, free electrons, and core electrons, respectively. The spectral shape of $S(k,\omega)$ depends on the electron density n_e, plasma temperature T, and ionization Z_f. Through variation of these parameters, best-fit values are obtained as given in Fig. 2. We find $n_e = (8.0 \pm 1.0) \times 10^{23}$ cm^{-3} and $T = (10 \pm 2)$ eV before shock collision. These values are consistent with

earlier measurements in isochorically heated [7] and single shock-compressed Be [8]. After shock collision, we find $n_e = (17.0 \pm 2.0) \times 10^{23}\,\mathrm{cm}^{-3}$ and $T = (15 \pm 2)\,\mathrm{eV}$. The ionization level was found to be $Z_f = 2.3$ before and after shock collision. Correspondingly, the mass densities before and after the shock collision are $\rho_1 = (5.2 \pm 0.7)\,\mathrm{g/cm}^3$ to $\rho_2 = (11.0 \pm 1.3)\,\mathrm{g/cm}^3$. Lee et al. [8] report $Z_f = 2.0$ for single compressed Be and $n_e = 7.5 \times 10^{23}\,\mathrm{cm}^{-3}$, hence slightly higher mass densities but still within our error bars. Our data do not support $Z_f = 2.0$ as shown by the dashed fit curves in Fig. 2, that clearly overestimate the far red wing of the scattering signal that is dominated by Compton scattering from bound electrons. Higher ionization levels are not likely because of the large ionization potential of $\sim 100\,\mathrm{eV}$ for Be^{2+} ions. This value already includes depletion of the ionization potential of $\sim 60\,\mathrm{eV}$ due to the dense plasma environment as estimated through the Stewart-Pyatt model [9].

4 Results for the adiabatic index

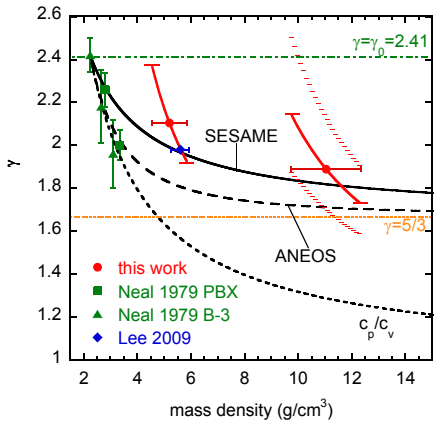

Fig. 3 (Color online) Adiabatic index γ for compressed Be as measured by X-ray Thomson Scattering (Red points). The blue diamond is calculated from compression data by Lee et al. (Ref. [8]). Squares and triangles at low compression are measurements of the sound speed γ by Neal (Ref. [10]). Analytical expressions for γ used in the SESAME EoS (solid curve) and the ANEOS model (dashed curve) and a linear scaling model for the heat capacity ratio c_p/c_v are shown using the lowest compression data by Neal as reference value, $\gamma_0 = 2.41$.

Using Eq. (17), we obtain $\gamma_1 = 2.1^{+0.3}_{-0.2}$ at $\rho_1 = (5.2 \pm 0.7)\,\mathrm{g/cm}^3$ and $\gamma_2 = 1.9^{+0.6}_{-0.3}$ at $\rho_2 = (11.0 \pm 1.3)\,\mathrm{g/cm}^3$ for the material after the collision. These results are shown in Fig. 3. The horizontal error bars on γ_2 result from the dependence on ρ_1 and ρ_2. Also shown are measurements of the sound speed gamma γ_1 for Be at low compression ratios by Neal [10]. Clearly, the sound speed gamma (Neal) and our data for the shock gamma differ at these high densities. Furthermore, differences in γ can be due to different temperatures; Neal does not state a temperature for his measurements. The continuous curves represent different models for γ as a function

of mass density [11]. These models are

$$\gamma(\rho) = \gamma(\rho_0)\frac{\rho_0}{\rho} + \frac{5}{3}\left(1 - \frac{\rho_0}{\rho}\right) , \tag{19a}$$

$$\gamma(\rho) = \gamma(\rho_0)\frac{\rho_0}{\rho} + \frac{5}{3}\left(1 - \frac{7}{5}\frac{\rho_0}{\rho} + \frac{2}{5}\left(\frac{\rho_0}{\rho}\right)^2\right) , \tag{19b}$$

$$\gamma(\rho) = 1 + (\gamma(\rho_0) - 1)\,\frac{\rho_0}{\rho} . \tag{19c}$$

The first model (19a) is implemented in the SESAME equation of state [12], the second (19b) is used in the ANEOS model [13], and the third can be used to model the density dependence of the heat capacity ratio c_p/c_v. Here, ρ_0 is a reference density, taken from the Neal data at lowest compression.

Our data are consistent with the linear model of Eq. (19a), whereas the Neal data for the sound speed γ support the quadratic model of Eq. (19b) that converges faster towards the high density limit $\gamma(\rho \to \infty) = 5/3$. Clearly, our data show the departure of the shock γ from the ratio of the heat capacities. At high densities our data seem to converge to the limit $5/3$, whereas the heat capacity ratio goes to $c_p/c_v = 1$.

In our analysis, we have assumed that effects due to x-ray and hot electron preheat of the target can be neglected. For the present laser parameters we estimated the hot electron temperature to remain below 3 keV using established models [14]. These hot electrons penetrate only the first $9\,\mu$m into the target and hence do not heat the central region of strong compression. X-ray preheat remains below 0.7 eV as estimated by calculating the total bremsstrahlung emission from the $2-3$ keV hot coronal plasma and absorption in the compressed Be.

5 Effect of the density dependence of γ on the compressibility

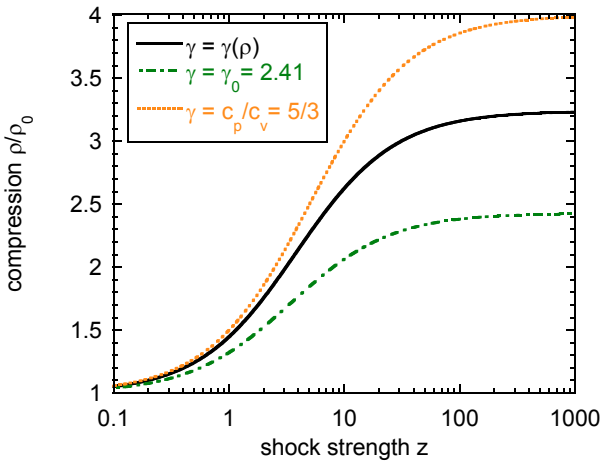

Fig. 4 (Color online) Compression as function of shock strength assuming various adiabatic indices: Black (solid) curve: liner SESAME model starting from $\gamma(\rho = \rho_0) = 2.4$; green (dash-dotted) curve: constant $\gamma = \gamma(\rho_0) = 2.4$; orange (dotted) curve: perfect gas heat capacity ratio $\gamma = c_p/c_v = 5/3$.

Fig. 4 shows the shock compression ratio ρ/ρ_0 for a single planar shock as a function of the shock strength z assuming three different shock gammas: The black curve was calculated using the linear SESAME model Eq. (19a) as plotted in Fig. 3. It assumes the lowest compression point measured by Neal as the reference point $\gamma_0 = 2.41$ and agrees with our measured data within the error bars. The green (dash-dotted) curve was calculated assuming a constant value for $\gamma = \gamma_0 = 2.41$ and the orange (dotted) curve takes the heat capacity ratio for

the perfect gas, $\gamma = c_p/c_v = 5/3$. The latter curve converges to the well known strong shock limit $\rho/\rho_0 \to 4$, whereas the models with higher γ remain below this limit. The linear scaling model predicts a limiting value of $\rho/\rho_0 \simeq 3.2$ at large z. Although the shock gamma within this model eventually reaches $\gamma = 5/3$, the maximum compression, being the solution of the equation $\rho/\rho_0 = f(z, \gamma(\rho/\rho_0))$ is always smaller than the limiting value. The limit assumed by the green curve is given by $\rho_{\max}/\rho_0 = (\gamma_0 + 1)/(\gamma_0 - 1) = 2.41$. These results show that the density dependence of the adiabatic index is crucial for the maximum single shock compression. Whereas a constant γ fixed at the value for solid Be predicts low compressibility, the often used heat capacity ratio overestimates the final compression. Our experimental results for γ support a moderate variation of γ with increasing density and the corresponding maximum compression is between the two aforementioned limits of constant γ.

6 Summary and Outlook

In summary, we have derived the shock wave kinetics for colliding shock waves for the general case that the shock gamma depends itself on density. The results were applied to infer γ for Be at two densities measured by X-Ray Thomson Scattering before and after the shock collision. The measured compression ratios of 2.8 and 5.9 yielded $\gamma_1 = 2.1$, and $\gamma_2 = 1.9$, respectively. These results are in good agreement with a linear scaling model that is implemented in the generator of the SESAME equation of state tables. Assuming this model to calculate $\gamma(\rho)$ for arbitrary densities, we obtain the compression ratio as a function of the shock strength. In the strong shock limit the density dependence of γ significantly reduces the maximum single shock compressibility. In our case, $\rho_{\max}/\rho_0 = 3.2$ instead of 4 as in the perfect gas model. On the other hand, taking $\gamma = \gamma_0$ fixed at the value for solid Be underestimates the maximum compression by a factor of ~ 0.8.

Acknowledgements

This work was performed under the auspices of the U.S. Department of Energy by Lawrence Livermore National Laboratory under Contract DE-AC52-07NA27344 and supported by LDRD grant 10-ER-050. C.F. acknowledges support by the Alexander von Humboldt-Foundation.

References

[1] S. H. Glenzer and R. Redmer, Rev. Mod. Phys. **81**(4), 1625–1663 (2009).
[2] D. C. Wilson, Phys. Plasma **42**(5), 1952 (1998).
[3] G. P. Horedt, Polytropes - Applications in Astrophysics and Related Fields (Kluwer Academic, Dordrecht, 2004).
[4] Y. Zel'Dovich and Y. Raizer, Physics of shock waves and high-temperature hydrodynamic phenomena (Dover Pubns, Mineola, New York, 2002).
[5] H. Motz, The Physics of Laser Fusion (Academic Press, London, 1979).
[6] J. MacFarlane, I. Golovkin, and P. Woodruff, J. Quant. Spectrosc. Radiat. Transfer **99**(1-3), 381–397 (2006).
[7] S. H. Glenzer, O. L. Landen, P. Neumayer, R. W. Lee, K. Widmann, S. W. Pollaine, R. J. Wallace, G. Gregori, A. Höll, T. Bornath, R. Thiele, V. Schwarz, W. D. Kraeft, and R. Redmer, Phys. Rev. Lett. **98**(6), 65002 (2007).
[8] H. J. Lee, P. Neumayer, J. Castor, T. Döppner, R. W. Falcone, C. Fortmann, B. A. Hammel, A. L. Kritcher, O. L. Landen, R. W. Lee, D. D. Meyerhofer, D. H. Munro, R. Redmer, S. P. Regan, S. Weber, and S. H. Glenzer, Phys. Rev. Lett. **102**(11), 115001 (2009).
[9] J. C. Stewart and K. D. Pyatt Jr., Astrophys. J. **144**(June), 1203 (1966).
[10] T. Neal, Determination of the gruneisenparameter for beryllium at 1.2 to 1.9 times standard density, in: High-Pressure Science and Technology, edited by K. D. Timmerhaus and M. S. Barber, AIRAP Conference Proceedings Vol. 1 and 2 (Plenum Press, New York, 1979).
[11] L. Davison, Fundamentals of Shock Wave Propagation in Solids (Springer, Heidelberg, 2008).
[12] S. Lyon and J. Johnson, Sesame: the los alamos national laboratory equation of state database, Database Technical report LA-UR-92-3407, Los Alamos National Laboratory, 1992.
[13] S. Thompson and . H.S. Lawson, Improvements in the chart d radiation- hydrodynamic code ih: Revised analytic equations of state, Tech. Rep. SC-RR-710714, Sandia National Laboratories, Albuquerque, NM, 1972.
[14] W. Kruer, The physics of laser plasma interactions (Westview Pr, Amsterdam, 2003).

A Second compression ratio as function of initial shock strength

Solving Eq. (14) for x_{12} yields

$$
\begin{aligned}
x_{12} = \Bigg\{ & (\gamma_0-1)(\gamma_1(3\gamma_2-1)+2){z_{01}}^2 + (2\gamma_2-\gamma_1(5\gamma_2+1)+\gamma_0(-4\gamma_2+\gamma_1(9\gamma_2-3)+2))z_{01} \\
& + 2\gamma_0(\gamma_1(3\gamma_2-1)-2\gamma_2) \\
& + \Bigg[\big(-(\gamma_0-1)(\gamma_1(3\gamma_2-1)+2){z_{01}}^2 + (5\gamma_2\gamma_1+\gamma_1-2\gamma_2+\gamma_0(\gamma_1(3-9\gamma_2)+4\gamma_2-2))z_{01} \\
& + 2\gamma_0(-3\gamma_2\gamma_1+\gamma_1+2\gamma_2)\big)^2 - 8(z_{01}+1)(z_{01}(\gamma_0-1)+2\gamma_0)(\gamma_1-1) \\
& \big((\gamma_0-1)(\gamma_1+2){z_{01}}^2 + 2\gamma_0 z_{01} + 3(\gamma_0-1)\gamma_1 z_{01} + 2\gamma_0\gamma_1\big)(\gamma_2-1)\gamma_2 \Bigg]^{1/2} \Bigg\} \\
& \Big\{ 2\big((\gamma_0-1)(\gamma_1+2){z_{01}}^2 + 2\gamma_0 z_{01} + 3(\gamma_0-1)\gamma_1 z_{01} + 2\gamma_0\gamma_1\big)(\gamma_2-1) \Big\}^{-1} . \qquad (20)
\end{aligned}
$$